

Out-of-equilibrium clock model at the verge of criticality

Marc Suñé and Alberto Imparato

*Department of Physics and Astronomy, University of Aarhus
Ny Munkegade, Building 1520, DK-8000 Aarhus C, Denmark*

(Dated: August 20, 2019)

We consider an out-of-equilibrium lattice model consisting of 2D discrete rotators, in contact with heat reservoirs at different temperatures. The equilibrium counterpart of such model, the clock-model, exhibits three phases; a low-temperature ordered phase, a quasi-liquid phase, and a high-temperature disordered phase, with two corresponding phase transitions. In the out-of-equilibrium model the simultaneous breaking of spatial symmetry and thermal equilibrium give rise to directed rotation of the spin variables. In this regime the system behaves as a thermal machine converting heat currents into motion. In order to quantify the susceptibility of the machine to the thermodynamic force driving it out-of-equilibrium, we introduce and study a dynamical response function. We show that the optimal operational regime for such a thermal machine occurs when the out-of-equilibrium disturbance is applied around the critical temperature at the boundary between the first two phases, namely where the system is mostly susceptible to external thermodynamic forces and exhibits a sharper transition. We thus argue that critical fluctuations in a system of interacting motors can be exploited to enhance the machine overall dynamic and thermodynamic performances.

PACS numbers:

The critical behaviour of equilibrium systems is well understood and supported by innumerable experimental observations. As a system approaches a critical point larger fluctuations in the local order parameter take longer time to emerge and longer time to decay. Also the response to a change in an external thermodynamic force can become significantly large. For example, in a gas at equilibrium with its liquid phase at the critical point a small change in the pressure produces a large density change, corresponding to a diverging compressibility. Other well known examples of diverging responses are the specific heat and the susceptibility of a critical 3D Ising model. Thus, criticality is characterized by wide fluctuations with diverging characteristic lengths, susceptibilities, and relaxation times.

One may wonder what is the fate of the equilibrium critical fluctuations if a disturbance is applied, that drives the system out of equilibrium. The system must be certainly removed from criticality, but at least for small non-equilibrium perturbation one may expect that fluctuations in the system persist and are still quite large. An even more interesting question is what happens to the diverging response of a critical system when such a non-equilibrium disturbance is applied. Is the response of a system close to its critical points enhanced with respect to the case where the system is non critical?

This question is particularly relevant in the context of stochastic and quantum thermodynamics, where several groups have addressed the issue of performance optimization in microscopic machines operating as engines and motors [1–4]. In particular, a few publications have shown that collective effects can enhance the efficiency of interacting microscopic machines. In models of interacting molecular motors the efficiency at maximum power of the many-motor system can be larger than in the single motor case [5–7]. Models of interacting work-to-work

transducers with all-to-all interaction exhibit a similar behaviour [8–10]. Furthermore, in ref. [11] the authors showed that the Carnot efficiency can be approached at finite output power in a system of microscopic interacting Otto engines when the working substances operate at the verge of a second order phase transition and the critical exponents satisfy some given constraints.

In this paper we investigate the role of criticality in the performance of thermal machines driven by temperature gradients: in particular we show that the out-of-equilibrium dynamic response of a system is maximal in the case in which the driving perturbation is applied at the verge of one of its critical points, i.e. when the system is most *susceptible* to equilibrium thermodynamic forces. We also demonstrate that phase transitions with different strengths are characterized by different dynamical responses, with the smoother equilibrium phase transition exhibiting the feebler out-of-equilibrium response.

Specifically we consider a model of interacting autonomous thermal motors, that converts steady state heat currents into mechanical motion. Autonomous motors are systems which continuously and cyclically convert one form of energy into another: such machines are characterized by the absence of one or more external agents that change their Hamiltonian or temperature. As such they are different from reciprocating engines that perform thermodynamic cycles, such as the Carnot, the Stirling and the Otto cycle, which have been widely investigated in the context of stochastic [12] and quantum [13] thermodynamics.

Our working tool will be the 2D clock model, consisting of $L \times L$ discrete rotors on a discrete 2D lattice, interacting through the Hamiltonian

$$H(\{\theta_i\}) = -\frac{k}{2} \sum_{\langle i,j \rangle} \cos[\theta_i - \theta_j + \varphi], \quad (1)$$

with $\theta_i = 2\pi n_i/N_s$, $n_i = 0, \dots, N_s - 1$, and with nearest neighbor interactions. We subdivide the lattice into two sublattices, each in contact with a heat bath at a different temperature $T_{\pm} = T_m \pm \Delta T$. Specifically we take a 2D square-lattice with periodic boundary conditions and L even, so that each “+” (“-”) rotator has 4 nearest neighbour “-” (“+”) rotators [14]. The model eq. (1) is chiral since we take $\varphi > 0$ when the spin i belongs to the “-” (cold) sublattice, and j belongs to the “+” (hot) one.

This model has the advantage that i) a single dimer consisting of only two spins interacting with the Hamiltonian (1) ($i = 1, j = 2$) has been shown to work as an autonomous motor: when $\varphi \neq n\pi/N_s$ and when in contact with two heat baths at different temperatures the spins rotate with a given average frequency, thus converting heat currents into motion and eventually into work [15, 16]; and ii) its non-chiral equilibrium counterpart ($\varphi = 0, \Delta T = 0$) exhibits a rich phase diagram with two second-order phase transitions [17].

In the following we use Monte Carlo (MC) simulations with Metropolis algorithm to first investigate the equilibrium properties of the model (1) ($\Delta T = 0$) and then its out-of-equilibrium dynamic properties, in particular the spin rotation rate for $\Delta T \neq 0$, and the heat rates exchanged by the system with the two reservoirs \dot{Q}_{\pm} . We define the angular velocity per spin as $\omega = (\omega_+ + \omega_-)/2$, where ω_{\pm} is the angular velocity per spin in the hot (cold) sublattice. The heat currents \dot{Q}_{\pm} along a single MC trajectory can be evaluated by sampling the total energy exchanged by the system with each of the two reservoirs along that trajectory.

We first study the equilibrium behaviour of the model (1), and we benchmark our results with those discussed by *Lapilli et al.* in [17], where the equilibrium properties of the non-chiral clock model ($\varphi = 0$) were extensively studied, and the model phase diagram was established by using MC simulations. In particular, as discussed by the authors, the model (1) with $4 < N_s < \infty$ and $\varphi = 0$ exhibits three phases: a low-temperature ordered and a high-temperature disordered phase, as in the Ising model, along with a quasiliquid intermediate phase. As $N_s \rightarrow \infty$ the ordered phase is suppressed, and the model becomes equivalent to the continuous XY model. In the following we set the energy scale by taking $k = 1$, and we notice that, because of the additional $1/2$ prefactor in our model (1), the temperature scale in the present paper is halved with respect to [17]. We label T_1^{eq} the equilibrium transition temperature between the low-temperature ordered and the quasi-liquid phase, and T_2^{eq} the equilibrium transition temperature between the quasi-liquid and the disordered phase. By using MC simulations, *Lapilli et al.* [17] provided an expression for the transition temperature T_1^{eq} as a function of the number of states for $N_s \geq 6$. They also reported an extended universality, which implies that the transition T_2^{eq} must be of the Berezinskii–Kosterlitz–Thouless (BKT) class, thus indistinguishable from $N_s = \infty$, for $N_s \geq 8$. Such equilibrium temperatures are reported in fig. 1 as lines, together with the

results from our MC simulations.

Similarly, we run equilibrium MC simulations ($\Delta T = 0$) for the chiral model $\varphi = \bar{\varphi}$, where we fix $\bar{\varphi} = \pi/(2N_s)$, and evaluate the equilibrium transition temperatures T_1^{eq} and T_2^{eq} , for different values of N_s . This is done through finite-size scaling analysis of the order parameter $\langle m \rangle \equiv \langle |\sum_i \exp(i\theta_i)| \rangle / L^2$ (the sum runs over all the rotators in the system), see [14, 17] for further details. The results for the two temperatures are also shown in fig. 1 and the agreement with the findings of [17] are excellent for $N_s \geq 8$. This can be understood by noticing that the chosen phase $\varphi = \bar{\varphi}$ decreases with N_s , so the equilibrium properties of the two models become equivalent in the limit of large N_s .

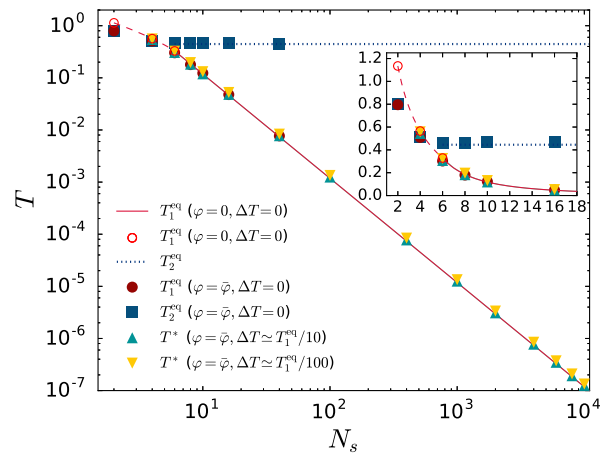


FIG. 1: Circles, squares, lines: equilibrium transition temperatures for the non-chiral ($\varphi = 0$) and the chiral clock model ($\varphi \neq 0$) as given by eq. (1). Lines: the expressions for T_1^{eq} (full) and T_2^{eq} (dotted) are taken from ref. [17]. Open circles: T_1^{eq} for $N_s \leq 6$, $\varphi = 0$, $\Delta T = 0$ [17], the dashed line is a guide to the eye for the results with $N_s \leq 6$. Full circles: numerical results for the first transition temperature T_1^{eq} as a function of N_s ($N_s \leq 40$) for the equilibrium model with $\varphi = \bar{\varphi}$. Squares: numerical results for the second transition temperature T_2^{eq} as a function of N_s , for the equilibrium model with $\varphi = \bar{\varphi}$. Triangles: temperature T^* that maximizes the dynamic susceptibility χ_ω in the out-of-equilibrium clock model with $\varphi = \bar{\varphi}$, see text and figure 3. Inset: Zoom of the small N_s region.

By using finite-size scaling analysis, we find that the critical exponent for the order parameter at the transition temperature T_1^{eq} is a decreasing function of the number of states, thus signaling a sharper transition at T_1^{eq} as N_s increases, see Supplemental material [14].

We now turn our attention to the model out-of-equilibrium properties. As for the case of two isolated spins interacting with the Hamiltonian (1) discussed in [16], also for the present model with L^2 spins there is a broken rotational symmetry when $\varphi \neq n\pi/N_s$, see [14].

Thus, as in the 2 spin model [15, 16], when the broken rotational symmetry is combined with a constant temperature gradient, the system is driven into an out-of-

equilibrium steady state, characterized by non-vanishing rotation rate per spin ω . The average angular velocity of the out-of-equilibrium system with $T_{\pm} = T_m \pm \Delta T$ is plotted in fig. 2 as a function of T_m for $N_s = 16$ and for different values of L and ΔT . We find that at large L the curve $\omega(T_m)$ becomes independent of L , see fig. 2-(a).

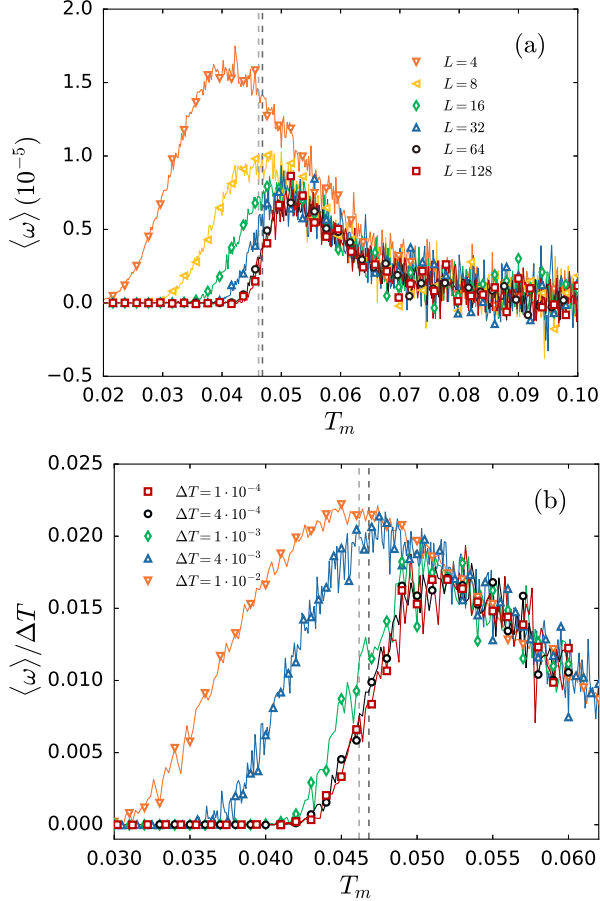


FIG. 2: (a) Average angular velocity per spin as a function of the mean lattice temperature T_m , for $N_s = 16$ and $\Delta T = 4 \cdot 10^{-4}$. (b) Ratio of the average angular velocity to the temperature gradient as a function of the mean lattice temperature T_m , for $N_s = 16$ and $L = 64$. The vertical dashed lines correspond to the equilibrium transition temperature T_1^{eq} for the clock model ($\varphi = 0$, light gray) [17], and the chiral clock model ($\varphi \neq 0$, dark gray), see fig. 1. In both panels we considered trajectories consisting of 1000 L^2 MC steps. In (a) the results are obtained by averaging over $(10^6, 2 \cdot 10^5, 5 \cdot 10^4, 8000, 8000, 1000)$ independent trajectories for the different system sizes ($L=4, 8, 16, 32, 64, 128$). The angular velocity is expressed in units of $1/(\text{number of MC steps per spin})$. In (b) the results are obtained by averaging over $(10^4, 8000, 200, 100, 100)$ trajectories for increasing ΔT .

In order to investigate the role of the critical fluctuations in a non-equilibrium system we introduce a *dynamic response* to a non-equilibrium perturbation, akin to the susceptibility in equilibrium systems. In equilibrium statistical mechanics the susceptibility of an order param-

eter ϕ with respect to its conjugate thermodynamic force f_ϕ reads $\chi_\phi = \partial \phi / \partial f_\phi|_{f_\phi=0}$. Similarly we introduce the susceptibility

$$\chi_\omega = \left. \frac{\partial \omega}{\partial \Delta T} \right|_{\Delta T=0}, \quad (2)$$

i.e., the response of the angular velocity with respect to the thermodynamic force that generates it. In the following we argue that this is the relevant quantity to characterize the out-of-equilibrium response of a system close to its critical points.

Given that $\omega = 0$ when $\Delta T = 0$ we can thus evaluate the response function (2) by numerical derivation $\chi_\omega \simeq \omega / \Delta T$. Unless otherwise stated, in the following we take $\Delta T \simeq T_1^{\text{eq}}/100$, for any N_s . Indeed when ΔT is as small as $T_1^{\text{eq}}/100$ the curves $\omega(T_m)/\Delta T$ collapse into a single curve, see fig. 2-(b).

The results for χ_ω as a function of T_m and for different values of N_s are shown in fig. 3-(a). We find that each curve $\chi_\omega(T_m, N_s)$ exhibits a peak at a temperature that depends on N_s . We indicate such a temperature T^* : it decreases as N_s increases. We refer to the value of the dynamic response function at its maximum as $\chi_\omega^* = \chi_\omega(T^*, N_s)$.

For any number of states N_s , we then compare the temperature T^* , as obtained for two values of ΔT , with the model equilibrium properties. In particular we compare the peak temperature with the two transition temperatures T_1^{eq} and T_2^{eq} . Interestingly, the temperature T^* (triangles in fig. 1) where $\chi_\omega(T_m, N_s)$ has its maximum χ_ω^* follows very closely the equilibrium transition temperature T_1^{eq} for $N_s \geq 4$ (full circles in fig. 1) with a relative difference $(T^* - T_1^{\text{eq}})/T_1^{\text{eq}} \lesssim 0.15$. This in turn implies that the points T^* with $N_s \geq 6$ lie near the curve given in [17] for the equilibrium temperature T_1^{eq} of the non-chiral model (full line in fig. 1). Accordingly, we conclude that the response of the system to the out-of-equilibrium perturbation ΔT is maximal when the perturbation is applied on the system in the proximity of one of its critical points: namely the transition point between the ordered and the quasiliquid phase. A more precise analysis on the correspondence between T^* and T_1^{eq} can be found in [14].

Unlike T_1^{eq} , the temperature T_2^{eq} does not give rise to any nonvanishing response, for any value of N_s . This might be seen as a consequence of the fact that the critical behaviour of the XY model at the BKT transition exhibits very weak singularities [18, 19]. For example the specific heat at T_{BKT} displays a singularity which is essentially unobservable [19].

In order to quantify the performance of the system, and its capability of transforming heat into rotational motion, we introduce the figure of merit $z = \langle \omega \rangle / \langle \dot{Q}_+ \rangle$, where $\langle \dot{Q}_+ \rangle$ is the steady state heat current entering the system from the hot reservoir. Interestingly, such figure of merit follows the same behaviour of ω and χ_ω , that is, it peaks around T^* . This result confirms that the optimal operational regime is achieved at $T_m \simeq T_1^{\text{eq}}$, see

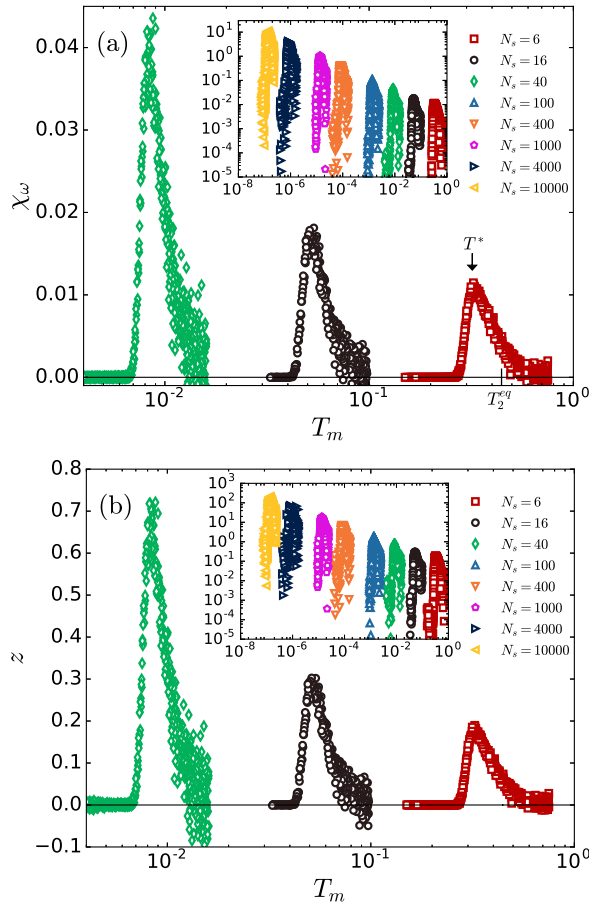


FIG. 3: (a) Out-of-equilibrium dynamical susceptibility χ_ω as a function of the mean lattice temperature T_m , for different number of states N_s , $L = 64$ and $\Delta T \simeq T_1^{\text{eq}}/100$. We consider 8000 independent trajectory, each consisting of 1000 L^2 MC steps, after the system has reached its steady state. For the system with $N_s = 6$ we indicate the temperature T^* for which χ_ω is maximum. The BKT temperature T_2^{eq} , indicated in panel (a), is independent of the number of states N_s , see fig. 1. Inset: χ_ω as a function of T_m for larger values of N_s . (b) Ratio of the average angular velocity to the heat current $z = \langle \omega \rangle / \langle \dot{Q}_+ \rangle$, as a function of the mean temperature. Inset: z as a function of T_m for larger values of N_s .

fig. 3-(b). This behaviour can be understood by noticing that while the angular velocity exhibits a somewhat abrupt peak around T^* (figs. 2 and 3-(a)), the heat current $\langle \dot{Q}_+ \rangle$ presents a smoother increase and decrease in that temperature range (data shown in [14]). Thus their ratio z exhibits the same peaking behaviour as ω and χ_ω .

Inspection of fig. 3 suggests that the height of the peak in both the dynamic susceptibility and the figure of merit is an increasing function of the number of states N_s . Thus as next point we investigate the dependency of χ_ω^* on N_s ; the results are plotted in fig. 4. Such a quantity increases linearly with the number of states, although with a slow rate. However, it is worth noticing that the velocity goes to zero as $N_s \rightarrow \infty$, as the rotational symmetry is re-

stored (see [14]), as can be seen in the lower inset of fig. 4. Therefore the continuous model $N_s \rightarrow \infty$ exhibits a diverging χ_ω^* , while $T^* \rightarrow 0$.

Interestingly, the increase of χ_ω^* is accompanied by the decrease of the order parameter critical exponent for the corresponding equilibrium system at T_1^{eq} , see [14]. We thus conclude that as the equilibrium transition becomes sharper, so does the corresponding out-of-equilibrium response.

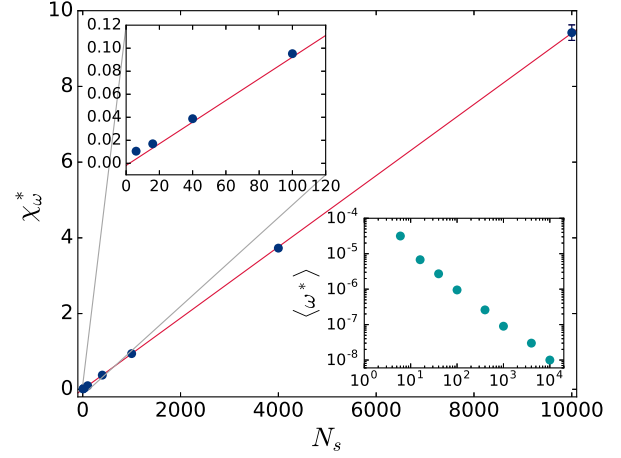


FIG. 4: Points: maximum value of the dynamical susceptibility χ_ω^* as a function of the number of states N_s , from the data in fig. 3-(a), as obtained with MC simulations for different number of states N_s , $L = 64$, and $\Delta T \simeq T_1^{\text{eq}}/100$. The full line is a linear fit to the data, with slope $b = (941.0 \pm 1.6) \cdot 10^{-6}$. Upper inset: zoom of the small N_s region. Lower inset: average angular velocity $\langle \omega^* \rangle$ at T^* as a function of the number of states.

To summarize, we have used the 2D chiral clock model to show that the optimal operational regime of a system of interacting autonomous motors occurs at the verge of a phase transition, in the limit of small driving thermodynamic forces. While the out-of-equilibrium response around the ordered-quasiliquid phase transition is noticeably sharp, the system response is vanishing in the other temperature ranges, in particular at the quasiliquid-disordered phase transition temperature. The same behaviour is found if one considers a figure of merit akin to a miles per gallon equivalent: the motors' "consumption" is most favorable around the strong phase transition. Interestingly, we find also that the response of the system increases, although slowly, with the number of states (directions) N_s in the clock model. This increase occurs while the corresponding phase transition for the equilibrium system becomes sharper. Our results provide strong evidence for the protocol that one has to follow in order to find the optimal working regime in systems of microscopic interacting motors: one has to first identify the system critical points, if any, and then systematically perturb the system at the verge of criticality.

Experimentally, a 2D system of interacting molecular rotors deposited on an hexagonal lattice have been re-

ported in [20]. That artificial molecular system represents a possible setup for an experimental realization of the model we have studied here.

Acknowledgments

This work was supported by the Danish Council for Independent Research and the Villum Foundation.

The numerical results presented in this work were obtained at the Centre for Scientific Computing, Aarhus <http://phys.au.dk/forskning/cscaa>.

-
- [1] G. Verley, M. Esposito, T. Willaert, and C. Van den Broeck, Nat. Comm. **5**, 4721 EP (2014), article.
 - [2] M. Polettini, G. Verley, and M. Esposito, Phys. Rev. Lett. **114**, 050601 (2015).
 - [3] M. Polettini and M. Esposito, EPL (Europhysics Letters) **118**, 40003 (2017).
 - [4] M. Suñé and A. Imparato, Journal of Physics A: Mathematical and Theoretical **52**, 045003 (2019).
 - [5] N. Golubeva and A. Imparato, Phys. Rev. Lett. **109**, 190602 (2012).
 - [6] N. Golubeva and A. Imparato, Phys. Rev. E **88**, 012114 (2013).
 - [7] N. Golubeva and A. Imparato, Phys. Rev. E **89**, 062118 (2014).
 - [8] A. Imparato, New Journal of Physics **17**, 125004 (2015).
 - [9] T. Herpich, J. Thingna, and M. Esposito, Phys. Rev. X **8**, 031056 (2018).
 - [10] T. Herpich and M. Esposito, Phys. Rev. E **99**, 022135 (2019).
 - [11] M. Campisi and R. Fazio, Nat. Comm. **7**, 11895 EP (2016), article.
 - [12] U. Seifert, Reports on Progress in Physics **75**, 126001 (2012).
 - [13] R. Kosloff, Entropy **15**, 2100 (2013), ISSN 1099-4300.
 - [14] See Supplemental Material for further details on the model equilibrium properties, on the correspondence between the equilibrium transition temperature and the maximal response temperature, and on the heat current.
 - [15] H. C. Fogedby and A. Imparato, EPL (Europhysics Letters) **119**, 50007 (2017).
 - [16] K. V. Hovhannisyan and A. Imparato, New Journal of Physics **21**, 052001 (2019).
 - [17] C. M. Lapilli, P. Pfeifer, and C. Wexler, Phys. Rev. Lett. **96**, 140603 (2006).
 - [18] J. M. Kosterlitz and D. J. Thouless, Journal of Physics C: Solid State Physics **6**, 1181 (1973).
 - [19] P. M. Chaikin and T. C. Lubensky, *Principles of Condensed Matter Physics* (Cambridge University Press, Cambridge, 1995).
 - [20] Y. Zhang, H. Kersell, R. Stefak, J. Echeverria, V. Iancu, U. G. E. Perera, Y. Li, A. Deshpande, K.-F. Braun, C. Joachim, et al., Nature Nanotechnology **11**, 706 EP (2016), article.
 - [21] K. Hovhannisyan and A. Imparato, arXiv **1806.08779** (2018).
 - [22] M. Plischke and B. Bergersen, *Equilibrium Statistical Physics* (WORLD SCIENTIFIC, 2006), 3rd ed.
 - [23] K. Binder and D. Heermann, *Monte Carlo Simulations in Statistical Physics* (Springer-Verlag Berlin Heidelberg, 2010), 5th ed.

Appendix A: Supplemental Material: Out-of-equilibrium clock model at the verge of criticality

1. Critical points for the chiral clock model at equilibrium

The Hamiltonian for the clock model in two dimensions eq. (1) with $\varphi = 0$ has a global symmetry $Z_{N_s}(H(\{\theta_i\}))$ is invariant under the transformations $\theta_i \rightarrow \theta_i + 2\pi n/N_s$. Thus one introduces the order parameter

$$\langle m \rangle \equiv \frac{\langle M \rangle}{L^2} = \frac{\langle |\sum_{j=1}^{L^2} \exp(i\theta_j)| \rangle}{L^2}, \quad (\text{A1})$$

that is invariant under the same symmetry group as the Hamiltonian in the high-temperature disordered phase. Besides this phase, the system exhibits two other phases for $N_s \geq 4$ (low-temperature ordered and quasi-liquid intermediate phase) and thus two critical points, as discussed in [17]: an ordered to quasi-liquid second-order phase transition and a quasi-liquid to disordered phase transition, that turns out to be of the Berezinskii-Kosterlitz-Thouless class for $N_s \geq 8$.

In the present paper we have considered the chiral model with $\varphi = \bar{\varphi}$. Similarly to the model with only two rotators discussed [21], also for the present model with L^2 rotors there is a broken rotational symmetry, in the sense that when $\varphi \neq n\pi/N_s$, one cannot find a discrete sublattice rotation l^+ (or l^-) such that $H(-\theta) = H(\{\theta_i^+ + 2\pi l^+/N_s, \theta_j^-\})$, $\forall \theta$ (or $H(-\theta) = H(\{\theta_i^+ + 2\pi l^-/N_s, \theta_j^-\})$), where $\theta = \{\theta^+, \theta^-\}$ is an arbitrary configuration of the system, and θ^+, θ^- are the configurations of the two sublattices, see fig. 5. This symmetry plays a fundamental role in the out-of-equilibrium model described in the main text. In the limit of $N_s \rightarrow \infty$ the model becomes the continuous XY model and the energy eq. (1) exhibits an O_2 symmetry, the group of rotations in a two-dimensional plane, and thus the model does not break the spatial symmetry discussed above. The consequence is that the angular velocity for the out-of-equilibrium model vanishes as $N_s \rightarrow \infty$ as discussed in the main text.

Through equilibrium MC simulations of the model we have evaluated the order parameter (A1) as a function

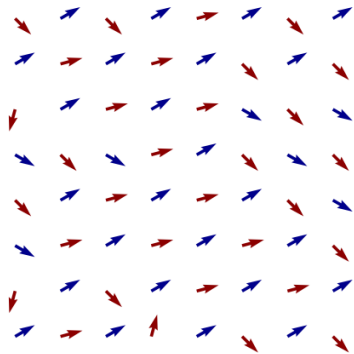


FIG. 5: Schematic representation of the 2D square-lattice model with $L = 8$ and periodic boundary conditions. Each “+” (“-”) rotator in red (blue) has 4 nearest neighbour “-” (“+”) rotators in blue (red).

of the temperature. Such a quantity is shown in fig. 6 for $N_s = 6$. Inspection of this figure indicates that the chiral model also exhibits two phase transitions. The order parameter for the standard clock model ($\varphi = 0$) is included for comparison.

The order parameter curves display two abrupt drops as the temperature is increased, from the low-temperature ordered phase ($\langle m \rangle \approx 1$) to the high-temperature disordered phase ($\langle m \rangle \approx 0$). In order to evaluate the corresponding transition temperatures we follow the approach used in [17]. To obtain the low-temperature transition T_1^{eq} , we evaluate the minimum of the temperature derivative of m for different system sizes L , $T_1^{eq}(L)$, see inset in fig. 6. We then use finite-size scaling analysis [22] to obtain $T_1^{eq} = T_1^{eq}(L \rightarrow \infty)$. For the high-temperature transition T_2^{eq} we exploit the Binder’s fourth order cumulant [23] of the order parameter,

$$U_L = 1 - \frac{\langle m^4 \rangle}{3\langle m^2 \rangle^2}. \quad (A2)$$

For $T > T_2^{eq}$ and assuming $L \gg \xi$, where ξ is the correlation length of the order parameter fluctuations, $U_L \propto L^{-d}$ (d is the dimension of the system). On the other hand, $U_L \rightarrow U_\infty = 2/3$ when $T < T_2^{eq}$ and $L \gg \xi$; and U_L varies weakly with T and L for $L \ll \xi$. Thus, the cumulant (A2) is scale invariant at the transition temperature, and therefore the transition temperature is given by the intersection between ratios of cumulants for different system sizes [23].

The critical temperatures as computed employing the aforementioned approaches for the equilibrium chiral clock model are depicted in fig. 1. The second equilibrium transition temperature is the same for both the chiral model ($\varphi \neq 0$) and the standard clock model ($\varphi = 0$), as

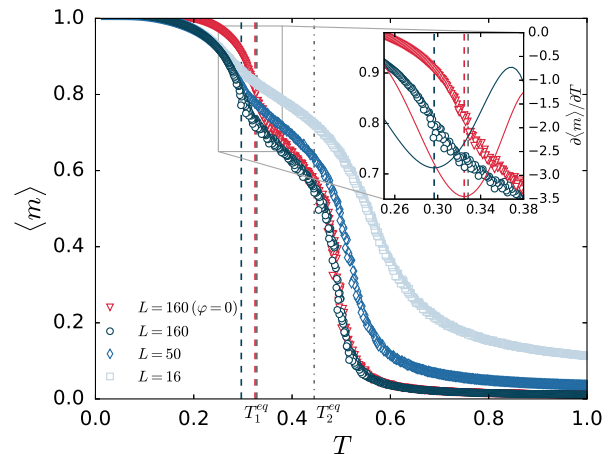


FIG. 6: Equilibrium order parameter for the standard clock model ($\varphi = 0$) and the chiral clock model ($\varphi = \bar{\varphi}$) as given by eq. (1) for some values of L , and with $N_s = 6$. The colored vertical dashed lines depict the low-temperature transition point as given by the minimum of the order parameter’s first derivative. The gray vertical dashed and dashed-dotted lines correspond respectively to the equilibrium transition temperatures T_1^{eq}, T_2^{eq} of the non-chiral ($\varphi = 0$) clock model obtained by Lapilli *et al.* [17]. Inset: Temperature derivative (full lines) of the equilibrium order parameter around the first transition temperature for $L = 160$ for both $\varphi = 0$ and $\varphi = \bar{\varphi}$. We consider 100 independent trajectories each consisting of 1000 L^2 MC steps following an equilibration run of 1000 L^2 MC steps.

it can be anticipated by the collapse of the corresponding order parameters curves in fig. 6. However, the order parameter curves deviate as they approach the lower-temperature critical point, thus the chiral clock model exhibits the first transition at a lower temperature. This deviation decreases with N_s as the two models become equivalent in this limit.

For different values N_s , and different sizes L , we evaluate the Binder’s fourth order cumulant for the energy [23]

$$V_L = 1 - \frac{\langle E^4 \rangle}{3\langle E^2 \rangle^2}, \quad (A3)$$

around the first transition temperature T_1^{eq} . The latent heat is proportional to $\lim_{L \rightarrow \infty} (2/3 - \min_T V_L)$ as discussed in [23]. We find that $\lim_{L \rightarrow \infty} \min_T V_L = 2/3$, which thus signals a second-order phase transition. We then proceed to evaluate the critical exponent β for the order parameter $(m - m_c) \propto (T - T_1^{eq})^\beta$, where m_c is the value of m at the transition point. We use finite-size scaling analysis of the order parameter for different sizes L [22] to obtain the critical exponent β . The results are shown in fig. 7, where we plot the exponent β as a function of N_s . We find that β is a decreasing function of the number of states N_s , indicating that the transition becomes sharper as the number of states increases. This result has to be compared with the results for the dynamical susceptibility in the main text, whose maximum

increases with N_s , see in particular fig. 4.

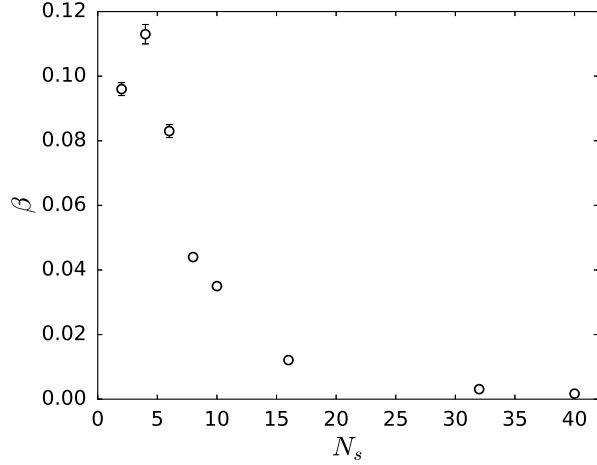


FIG. 7: Equilibrium chiral clock model ($\varphi = \bar{\varphi}$): critical exponent for the order parameter at the low temperature phase transition point T_1^{eq} , as a function of the number of states N_s .

2. Correspondence between T^* and T_1^{eq}

The temperature at which the susceptibility eq. (2) is maximal T^* has been shown to depend on ΔT , see fig. 2-(b). Its behavior when varying the number of states N_s is depicted in fig. 1, where two different temperature gradients are considered $\Delta T \simeq T_1^{\text{eq}}/10$ and $\Delta T \simeq T_1^{\text{eq}}/100$. The maximum temperature T^* follows closely the equilibrium clock model transition temperature T_1^{eq} for both $\varphi = 0, \bar{\varphi}$, yet some discrepancy is already anticipated in fig. 1. In order to compare T^* and T_1^{eq} a more convenient representation of the data in fig. 1 is to plot the relative deviation of the maximum susceptibility's temperature T^* with respect to the equilibrium transition temperature T_1^{eq} as a function of the number of states, see fig. 8.

When decreasing the number of states, and hence when the standard clock model begins to deviate from the chiral one, the maximal susceptibility temperature T^* tends to approach the corresponding equilibrium temperature T_1^{eq} . Yet a deviation persists, so that T^* is always above T_1^{eq} when the temperature gradient is small. On the other hand, the difference between T^* and T_1^{eq} is larger for the smaller ΔT considered, in agreement with the results plotted in fig. 2-(b).

3. Heat current

The heat currents \dot{Q}_{\pm} along a single MC trajectory can be retrieved by exploiting the conservation of energy: the energy rate exchanged by each of the two sublattices with the corresponding heat reservoir must amount to the

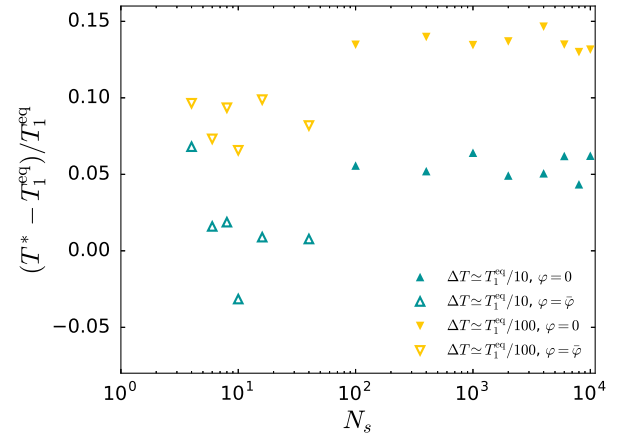


FIG. 8: Deviation of the temperature at the maximal susceptibility T^* respect to the equilibrium clock model [17] (filled triangles) and the equilibrium chiral clock model (open triangles) lower critical temperature T_1^{eq} , for two different thermodynamic forces $\Delta T \simeq T_1^{\text{eq}}/10$ (green upward triangles) and $\Delta T \simeq T_1^{\text{eq}}/100$ (yellow downward triangles); $L = 64$.

energy variation due to the sublattice's spin transitions, given by eq. (1). Accordingly, the sum of the two heat currents should sum up to zero on average.

The heat current as a function of T_m for a given value of N_s reaches a maximum which depends on N_s , similarly to what happens for the angular velocity, see fig. 9-(a). Yet a close inspection shows that the curve reaches such a maximum at a larger temperature than T^* , see fig. 9-(b), where we compare the angular velocity $\langle \omega \rangle$ and the heat current $\langle \dot{Q}_+ \rangle$ for two values of N_s . The angular velocity exhibits a sudden rise/decrease around T^* . The heat current has a somewhat smoother rising and decreasing behaviour around the maximum. We see that the system still transports heat ($\langle \dot{Q}_+ \rangle \neq 0$) in the range of T_m where $\langle \omega \rangle$ vanishes due to the wandering of the rotators between their different positions, although this movement does not result in a net rotation. The combination of the abrupt variation of $\langle \omega \rangle$ around T^* together with the smoother behaviour displayed by $\langle \dot{Q}_+ \rangle$ implies that the figure of merit z (i.e. their ratio) follows the same behaviour of the angular velocity and peaks around T^* , see fig. 9-(c).

The heat current's peak at $T \gtrsim T^*$ is nonetheless not unique; a second maximum (possibly larger than the one discussed above) is found above T_2^{eq} , see fig. 10-(a), although only for small N_s . The maxima displayed by the curves $\langle \dot{Q}_+ \rangle / \Delta T$ close to the transition temperature T_1^{eq} is constant with respect to the number of states N_s , see fig. 10-(a), at variance with the mechanical current response function as defined in eq. 2, see also fig. 3-(a) in the main text. A rescaling of the x -axis thus leads to a collapse of the heat current curves around the transition temperature T_1^{eq} , see fig. 10-(b). Both the mechanical and thermal currents are expected to be linear with respect to the thermodynamic force when ΔT is small, as

it is in our case, according to the Onsager reciprocal relations. However, we find a different scaling behavior of

the two currents with respect to N_s , as suggested when comparing fig. 3-(a) and fig. 10-(a).

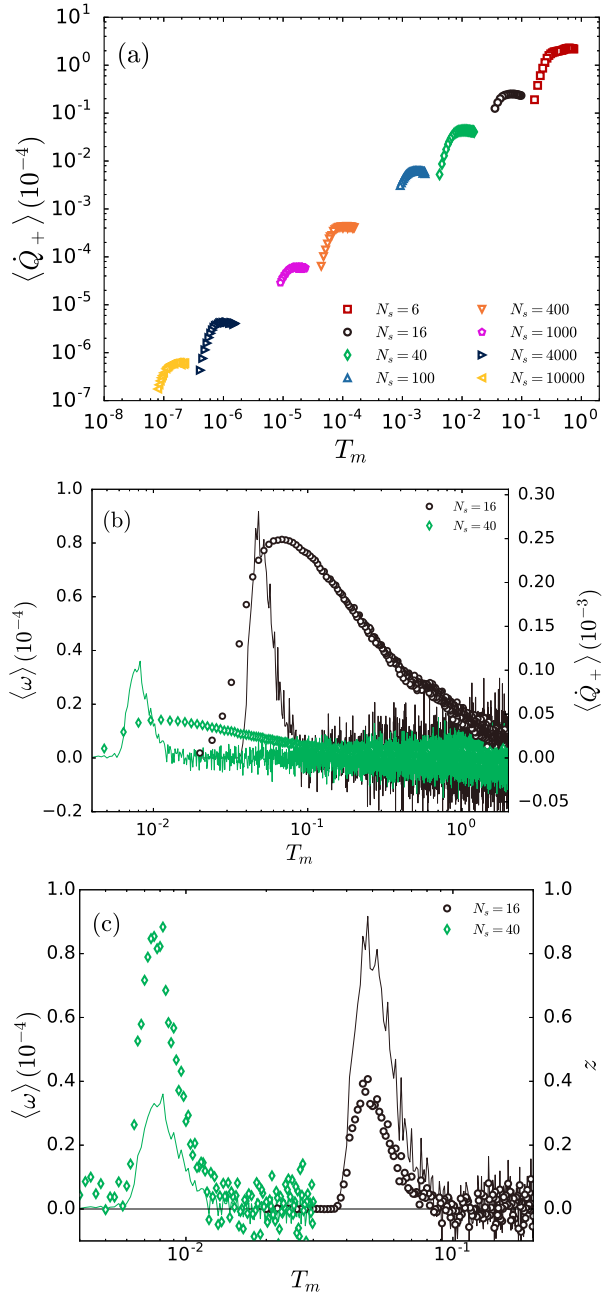


FIG. 9: (a) Average steady-state heat current flowing into the system from the hot reservoir $\langle \dot{Q}_+ \rangle$ as a function of the mean lattice temperature T_m for different number of states N_s , $L = 64$ and $\Delta T \simeq T_1^{\text{eq}}/100$, corresponding to the simulations in fig. 3. (b) Average steady-state velocity $\langle \omega \rangle$ (lines, left y-axis) and heat current (symbols, right y-axis) flowing into the system from the hot reservoir as a function of the mean lattice temperature T_m for $N_s = 16, 40$, $L = 64$ and $\Delta T \simeq T_1^{\text{eq}}/10$. (c) Comparison between the average steady-state velocity (lines, left y-axis) and the corresponding figure of merit $z = \langle \omega \rangle / \langle \dot{Q}_+ \rangle$ (symbols, right y-axis), same parameters as in panel (b).

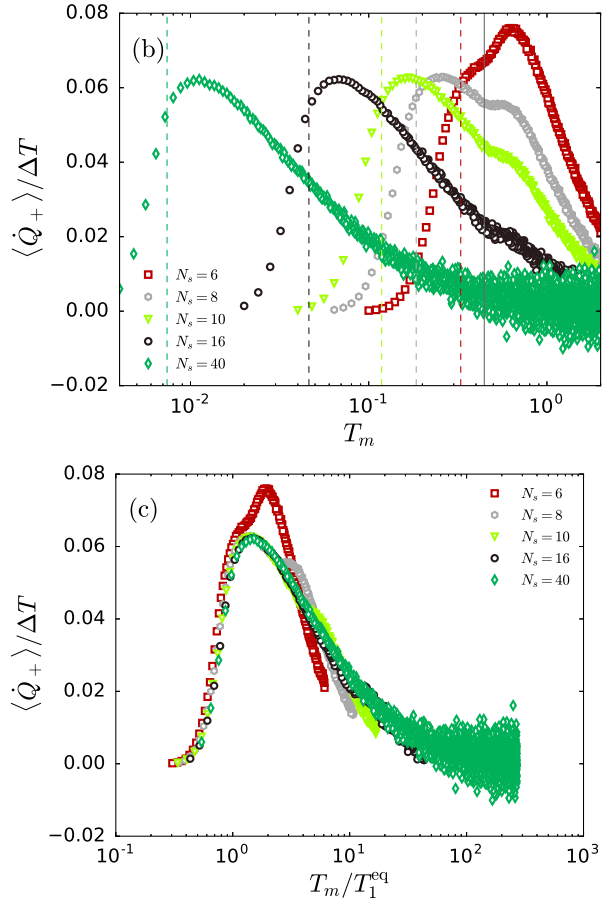


FIG. 10: Ratio of the average heat current flowing into the system from the heat reservoir to the out-of-equilibrium perturbation ΔT as a function of the mean temperature T_m (a) and as function of T_m/T_1^{eq} (b) for different number of states N_s , $L = 64$ and $\Delta T \simeq T_1^{\text{eq}}/10$. The coloured dashed lines and the full grey line in (a) label respectively the equilibrium transition temperatures $T_1^{\text{eq}}(N_s)$ and $T_2^{\text{eq}}(N_s \geq 8) = T_{\text{BKT}}$ for the standard clock model ($\varphi = 0$) as obtained in [17].

